The Astrophysical Journal, 721:1–8, 2010 ??? doi:10.1088/0004-637X/721/1/1
© 2010. The American Astronomical Society. All rights reserved. Printed in the U.S.A.

SUNSPOT ROTATION, FLARE ENERGETICS, AND FLUX ROPE HELICITY: THE HALLOWEEN FLARE ON 2003 OCTOBER 28

Maria D. Kazachenko, Richard C. Canfield, Dana W. Longcope, and Jiong Qiu
Montana State University, Bozeman, MT 59715, USA; kazachenko@physics.montana.edu
Received 2010 March 25; accepted 2010 August 24; published 2010 ???

ABSTRACT

Q1

We study the X17 eruptive flare on 2003 October 28 using MDI observations of photospheric magnetic and velocity fields and *TRACE* 1600 Å images of the flare in a three-dimensional model of energy buildup and release in NOAA 10486. The most dramatic feature of this active region is the 123° rotation of a large positive sunspot over 46 hr prior to the event. We apply a method for including such rotation in the framework of the minimum current corona model of the buildup of energy and helicity due to the observed motions. We distinguish between helicity and energy stored in the whole active region and that released in the flare itself. We find that while the rotation of a sunspot contributes significantly to the energy and helicity budgets of the whole active region, it makes only a minor contribution to that part of the region that flares. We conclude that in spite of the fast rotation, shearing motions alone store sufficient energy and helicity to account for the flare energetics and interplanetary coronal mass ejection helicity content within their observational uncertainties. Our analysis demonstrates that the relative importance of shearing and rotation in this flare depends critically on their location within the parent active region topology.

Key words: Sun: activity – Sun: coronal mass ejections (CMEs) – Sun: flares – Sun: magnetic topology – Sun: surface magnetism – Sun: sunspots

Online-only material: color figure

1. INTRODUCTION

In this work, we study pre-flare storage of energy and helicity and their release through magnetic reconnection in the Halloween flare on 2003 October 28. This X17 flare took place in NOAA 10486, an active region of complex magnetic structure that had for several days undergone both shearing and rotational motions. Figure 1 (top panel) shows the GOES 1–8 Å X-ray flux curve from 2003 October 26 to 28. On the day of the flare, the X-ray flux started growing at 9:51 UT and peaked at X17 level at 11:10 UT. About 40 minutes before the X17 flare, the observed phenomena included a filament eruption seen in EUV, *TRACE*, and H_α images. Even though this filament eruption and the X17 flare involved the same magnetic inversion line, it is not clear whether they were related to each other because of the time difference (Su et al. 2006). It is worth noting that Zuccarello et al. (2009) interpret these observations as a chain of events leading to the X17 flare. In this paper, we focus on the X17 event alone.

The Halloween flare has interested many authors (see, e.g., Pick et al. 2005; Hurford et al. 2006; Mandrini et al. 2006; Schmieder et al. 2006; Su et al. 2006; Li et al. 2007; Trottet et al. 2008; Zhang et al. 2006; Zuccarello et al. 2009). Our unique contribution to this large amount of work is the *quantitative* modeling of the storage of energy and helicity due to motions of photospheric magnetic fields, including the effects of *both* shearing and sunspot rotation.

The key to this quantitative modeling is the minimum current corona (MCC) model (Longcope 1996, 2001). It builds on the CSHKP two-ribbon flare model where reconnection creates a flux rope, which is ejected in a coronal mass ejection (CME). The MCC model is a non-potential self-consistent analytical model of the quasi-static evolution of the three-dimensional coronal field due to photospheric motions. It characterizes the coronal field purely in terms of how it interconnects photospheric unipolar magnetic source regions, called partitions. The amount of the total potential flux interconnecting regions $\mathcal{R}_a$ and $\mathcal{R}_b$, called the domain flux $\psi^{(v)}_{a/b}$, can be computed from the magnetogram divided into partitions. Replacing each partition with a single magnetic point charge located at the centroid of the partition, as we choose to do, results in values of $\psi^{(v)}_{a/b}$ that are only slightly different from the actual domain flux (Longcope et al. 2009). As the magnetic charges move, they will be interconnected by various values of the domain fluxes, $\psi^{(v)}_{a/b}(t)$. The MCC model assumes that the field evolves through a sequence of flux-constrained equilibria (FCE) defined as the states of minimum magnetic energy subject to constraints on all its domain fluxes. Each FCE field includes currents only on the intersections between its separatrices, called separators. These are the only locations at which current is required by the constraints. Under the assumption that no reconnection, flux emergence, or cancellation occur during the magnetogram sequence, the domain fluxes could not have changed and the field could not have remained in a potential state. In this way, the lack of reconnection leads to storage of free magnetic energy, energy above that of the potential field, which could then be released by reconnection. To achieve the maximum energy release, the field inside the flaring domains would need to relax to its potential state. Our working hypothesis is that the transfer of this flux through reconnection is responsible for the flare. The physical picture of the MCC is that stress is built up on the active region's coronal magnetic separators due to the observed motions of the photospheric magnetic field and is removed by reconnection in eruptive flare events. The stress starts building up right after the end of a large flare, when the magnetic field becomes fully relaxed; thus, to model the stress released in the flare, we must pick an active region which had a previous flare before the flare of study. The MCC model allows us to quantify the energetic and topological consequences of changes of connectivity by reconnection and the helicity transfer between magnetic domains.

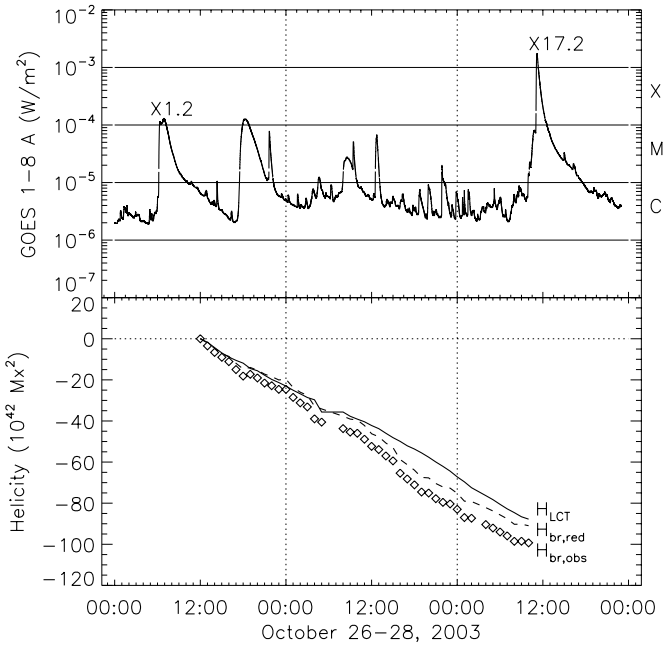

Figure 1. GOES 1–8 Å light curve (top) and the integrated helicity injected by the photospheric motions (bottom). In the bottom panel, the solid curve is the result of applying Equation (1) to the LCT velocity field ($H_{\rm LCT}$). The ◇'s show the braiding helicity injected by the motions of the point charges using Equation (2) ($H_{\rm br,obs}$). The dashed line is the braiding helicity for the reduced model ($H_{\rm br,red}$).

Such slow energy storage is often inferred observationally using the time-rate-of-change of relative helicity flux as a proxy (Berger & Field 1984; van Driel-Gesztelyi et al. 2003). The time-rate-of-change of relative helicity due to photospheric motions is given by a surface integral involving velocity and magnetic field. For brevity, we hereinafter refer to this total integral as the *helicity flux*, recognizing that there is no spatially resolved density capable of revealing the local distribution of helicity changes (Pariat et al. 2005). The helicity flux integral can be decomposed into a sum of terms corresponding to distinct types of photospheric motion and modes of energy storage. A term involving the vertical velocity corresponds to the injection of helicity and energy by emergence of current-carrying flux. Terms involving the horizontal velocity are further separated into braiding and spinning contributions (Welsch & Longcope 2003; Longcope et al. 2007b). The braiding term captures energy and helicity injected as photospheric magnetic regions move relative to one another, while the spinning term captures energy and helicity when they rotate.

This is the third in a series of studies we have carried out on specific large eruptive flares, analyzing observations of the structure and evolution of photospheric magnetic fields to quantitatively estimate the amount of coronal helicity and energy released by reconnection.

In Paper I, Longcope et al. (2007a) applied the MCC model to the X2 flare on 2004 November 7, in NOAA 10696. They partitioned a 40 hr sequence of magnetograms to create a model of the evolving AR photospheric magnetic field as moving point charges. Because the magnetogram sequence showed only shear motions and no sunspot rotation (Longcope et al. 2007b), all partitions could be represented by magnetic point charges. Longcope et al. (2007a) quantified the evolution of the coronal fluxes in the flux domains interconnecting these point charges, related them to the magnetic separators of the three-dimensional topological skeleton of the AR, and applied the MCC model to estimate the stored energy and helicity. They found that the amount of flux that would need to be reconnected during the flare in order to release the stored energy compared favorably with the flux swept up by the flare ribbons measured using *TRACE* 1600 Å images. Full details of the separator reconnection sequence and the application of the MCC model to this event are given in Paper I.

In Paper II, Kazachenko et al. (2009) applied the MCC model to the M8.0 flare on 2005 May 13, in NOAA 10759. The pre-flare evolution of the photospheric magnetic field of this AR differed from that studied in Paper I in one important respect: it showed obvious sunspot rotation. These authors therefore incorporated rotation into the MCC model by using a three-point (quadrupolar) representation of the partition that corresponded to the rotating sunspot, rather than a single point. They found that the rotation of the sunspot produced three times more energy and magnetic helicity than the non-rotating case, and the inclusion of sunspot rotation in the analysis brought the model into substantial agreement with observations. Discussion of previous work on sunspot rotation and details of the incorporation of the quadrupolar representation into the MCC model are given in Paper II.

In this work, we apply the analysis methods developed in Papers I and II to the Halloween flare. Using the MCC model and a quadrupolar representation of the large rotating sunspot, we calculate the amount of flux, energy, and helicity transferred by reconnection. Interestingly, in contrast to Paper II, we find that the fast rotation of the large sunspot in NOAA 10486 does not significantly change the total flare free energy and flux rope magnetic helicity compared to the non-rotating case.

This paper is organized as follows. In Section 2, we present the magnetogram sequence and partitioning used in the study. In Section 3, we discuss the helicity injected by the photospheric motions, the rotation of the large positive sunspot, and the way we incorporate it in our model. In Section 4, we calculate the reconnection flux from the model and compare it with the measured flux from the flare observations. Section 5 lists properties of the separators found in the coronal topology at the time of the flare. In Section 6, we evaluate the role of sunspot rotation. Finally, we summarize our results in Section 7.

2. THE MAGNETOGRAM SEQUENCE

Our magnetic field data consist of a sequence of SOI/MDI full-disk magnetograms (2″, level 1.8, Scherrer et al. 1995). As the start time of the sequence, we take t_0 = 2003 October 26 12:00 UT, after the X1.2 flare, which occurred in NOAA 10486 on October 26 05:57 UT. As the end time of the sequence, we take $t_{\rm flare}$ = 2003 October 28 10:00 UT, one hour before the X17 flare peak time. We chose $t_{\rm flare}$ and t_0 so that the magnetic field measurements do not contain artifacts associated with the onset of the flare brightening (Schrijver et al. 2006; Qiu & Gary 2003). As a result, we form an hourly sequence of 45 low-noise magnetograms, which covers 46 hr of the stress buildup removed by the X17 flare on October 28 11:10 UT.

To estimate the amount of flux topologically changed during the X17 flare, we must divide the pre-flare photospheric field into a set of evolving unipolar partitions. Firstly, for all successive pairs of magnetograms, we use a Gaussian apodizing window of 7″ to derive a local correlation tracking (LCT) velocity (November & Simon 1988). We then take a magnetogram at $t_{\rm flare}$ and group pixels, exceeding a threshold $B_{\rm thr}$ = 60 G downhill from each local maximum, into individual partitions

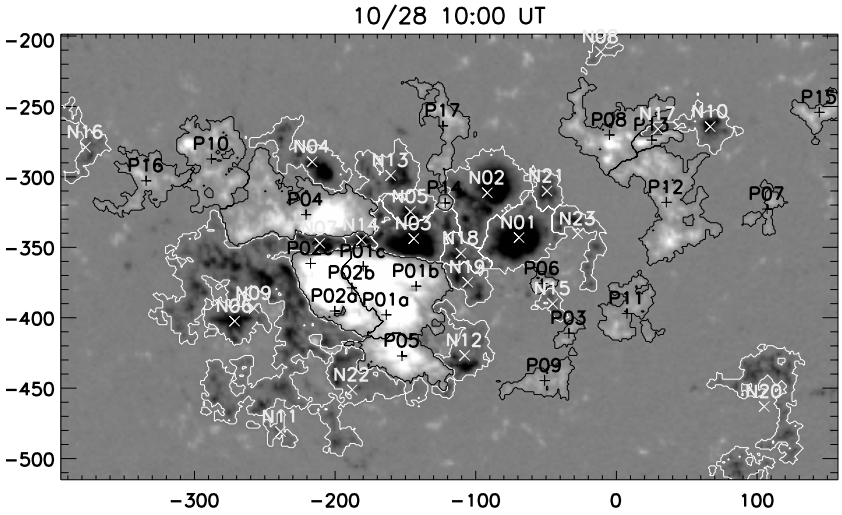

Figure 2. Positive (P) and negative (N) polarity partitions for NOAA 10486 on October 28 10:00 UT, one hour before the start time of the X17 flare (see Section 2). The gray-scale magnetogram shows the magnetic field scaled from −1000 G to 1000 G. The partitions are outlined and the centroids are denoted by +'s and x's (positive and negative, respectively). Axes are labeled in arcseconds from disk center.

(Barnes et al. 2005). We combine partitions by eliminating any boundary whose saddle point is less than 700 G below either maximum it separates. Each partition is assigned a unique label which it maintains through the sequence. To accomplish this, we generate a reference partitioning by advecting the previous partitions to the present time using the LCT velocity pattern. Of course, partitions at the present time do not perfectly match the previous partitions. Hence, we assign each partition the label of the reference partition which it most overlaps. We find that performing the process in reverse chronological order backward from $t_{\rm flare}$ provides the most stable partitioning. Figure 2 shows the spatial distribution of these partitions at $t_{\rm flare}$.

Each magnetic partition a is represented by a magnetic point charge (or magnetic point source) with centroid, $\mathbf{x}_a$, and magnetic flux, Φ_a. The magnetic point charges found in this way exhibit so little variation in flux from one magnetogram to the next in the sequence that we use what we call the *reduced model*, in which all individual partition fluxes are held strictly constant and equal to the fluxes at $t_{\rm flare}$.

The overall evolution of the active region can be characterized by the flux of relative helicity into the corona, $\dot{H}_{\rm LCT}$. This can be calculated from the LCT velocity $\mathbf{u}$ (Berger & Field 1984; Chae 2001; Démoulin & Berger 2003) from the integral

$$\dot{H}_{\rm LCT} = -2 \int_{z=0} [\mathbf{u} \cdot \mathbf{A}_P]\, B_z\, d^2x, \qquad (1)$$

over the magnetogram, where $\mathbf{A}_P$ is the vector potential field for the curl-free (potential) magnetic field matching $B_z(x, y)$. The motions of the magnetic point charges alone contribute a braiding helicity flux (Berger & Field 1984; Welsch & Longcope 2003; Longcope et al. 2007a):

$$\dot{H}_{\rm br} = -\frac{1}{2\pi} \sum_a \sum_{b \neq a} \Phi_a \Phi_b \frac{d\theta_{ab}}{dt}, \qquad (2)$$

where θ_{ab} is the polar angle of the separation vector, $\mathbf{x}_a - \mathbf{x}_b$, connecting two magnetic point charges a and b. $\dot{H}_{\rm br}$ quantifies the amount of helicity added to the coronal field as its footpoints are moved about one another. Integrating each of these expressions from t_0 to $t_{\rm flare}$ shows a steady flux of negative helicity until it reaches maximum value at approximately $t_{\rm flare}$ (see Figure 1, bottom panel). The braiding helicity fluxes of the point charges with observed fluxes ($H_{\rm br,obs}$, diamonds) and of the reduced model ($H_{\rm br,red}$, dashed curve) closely match the actual helicity flux ($H_{\rm LCT}$, solid line). This gives some confidence that the centroid motions of our source regions capture the likely driver for the flare: helicity injection.

3. SUNSPOT ROTATION

3.1. Observations of Rotation

Observations of the large, positive sunspots P02 and P01 in MDI full-disk intensity images show them to be rotating around their umbral centers during 2003 October 25–30 (Zhang et al. 2006). To find the rotation rate, Zhang et al. (2006) measure the angular displacement of the sunspots between two successive days and look at the fluctuations of the umbra profile on the MDI intensitygrams. MDI magnetograms of the same temporal and spatial resolution are not useful for rotation measurements since they exhibit lower contrast of the features in the penumbra than intensitygrams. Using rotation rates from Zhang et al. (2006), we find that in 46 hr, between t_0 and $t_{\rm flare}$, P02 rotated by 123°, whereas the southern part of P01 rotated by only 12°.

3.2. Representation Using Point Charges

Since P02 is one of the largest and fastest rotating partitions in the AR, a large fraction of the total helicity flux, and possibly the energy storage, is associated with it. Clearly, it is not possible to model the helicity injected by a spinning partition with a single point charge. In order to model helicity and energy storage due to such motion, we represent P02 with three separate point sources P02a, P02b, and P02c of equal flux. Rather than constraining connection to P02 as a whole, we constrain connections to each source separately. Following Paper II, we locate the three point sources about an ellipse so as to match the first three terms of the multipole expansion of the true field of P02 (see Figure 2). To model the rotation, we move the triad of point charges about the ellipse injecting braiding helicity flux into P02 beyond what the single-charge model would yield. The internal braiding helicity can be used to account for observed spin helicity from P02 using the method described in Paper II.

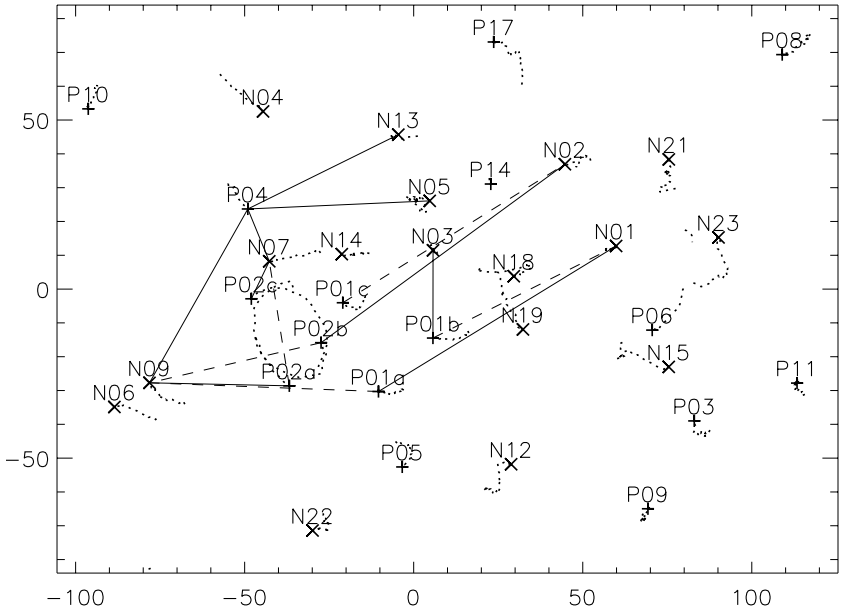

Figure 3. Motions of the labeled poles in the pre-flare magnetogram sequence, see Section 3. The dotted curves show the paths taken by the poles in 46 hr in the co-rotating plane from October 26 12:00 UT to October 28 10:00 UT, ending at the corresponding pole labels. The paths of $P02_{a,b,c}$ clearly show the CCW rotation of this spot. The solid (dashed) lines connect each pole pair whose potential-field domain flux $\psi^{(v)}_{a/b}$ has increased (decreased) by more than 0.5×10^{21} Mx in 46 hr between October 26 12:00 and October 28 10:00 UT, $|\Delta\psi^{(v)}_{a/b}| > 0.5 \times 10^{21}$ Mx.

Although we find that the helicity injected by the rotation of the largest partition P01 is negligible, we nevertheless chose to represent P01 with three rather than one point source. We do this since multipole expansion improves the accuracy of coronal extrapolation and enables a more in-depth analysis of the photospheric magnetic field changes. We neglect the rotation of P01 for two reasons. Firstly, P01's rotation rate is more than 10 times smaller than that of P02. Secondly, the rotation is observed only in the southern part of P01, which lies farther from the part of the polarity inversion line where the flare occurs. We find that neglecting the rotation of P01 leads to an error of 6% maximum in the total braiding helicity flux $\Delta H_{\rm br}$.

Figure 3 shows the motions of the point charges which lead to helicity accumulation. Note the representation of P01 with three poles which do not rotate and P02 with three poles that do. The importance of the plotted P02 rotation as a source of helicity injection into the whole active region is demonstrated by comparing the braiding helicity flux from two different models. In the first, P02a, P02b, and P02c *do not rotate* and move only so as to reproduce the centroid motion of P02 alone; the time-integrated braiding helicity flux (Equation (2)) of the whole active region is

$$\Delta H_{\rm br} = -9.0 \times 10^{43}\,{\rm Mx}^2. \quad (3)$$

In the second, P02a, P02b, and P02c *rotate* reproducing the rotation rate derived from MDI intensitygrams ($2.^\circ67\,{\rm hr}^{-1}$); the time-integrated braiding helicity flux is

$$\Delta H_{\rm br} = -14 \times 10^{43}\,{\rm Mx}^2. \quad (4)$$

Evidently, the rapid motion of the three poles of P02 relative to the other poles injects almost twice as much helicity as the case where the three poles do not rotate. Clearly for meaningful helicity calculations of the whole active region, we must take rotation into account. However, we show below that for the helicity of the flare itself the rotation is not important.

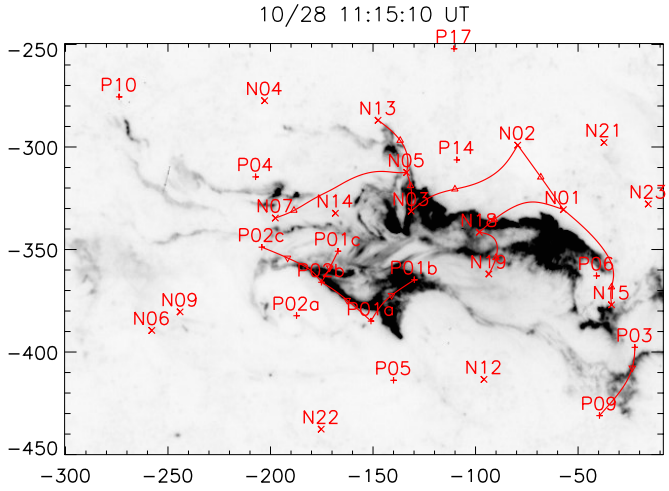

Figure 4. *TRACE* 1600 Å image, plotted as reverse gray scale, with elements of the topological skeleton superimposed. The skeleton calculated for October 28 10:00 is projected onto the sky after its tangent plane has been rotated to the time of the *TRACE* observations (11:15 UT). Positive and negative sources are indicated by +'s and x's, respectively. The triangles represent the labeled null points. The curved line segments show spine lines associated with the reconnecting domains, as discussed in Section 4. Axes are in arcseconds from disk center.

(A color version of this figure is available in the online journal.)

4. RECONNECTION FLUX: MODEL VERSUS OBSERVATIONS

To find the theoretical estimate of the amount of flux reconnected in the flare, we must first determine the domains where the flare occurred, the so-called flaring domains. Figure 4 shows a superposition of the elements of the topological skeleton at $t_{\rm flare}$ onto the *TRACE* 1600 Å flare ribbon image at 11:15 UT. The topological skeleton (poles, null points, spines, etc.) describes the potential field geometry found for the observed

magnetic charge distribution. The spines (solid lines) that are associated with ribbons form the footprint of a combination of separatrices which overlay the flaring domains. The overlay suggests that the southern ribbon is associated with the spines connecting flaring point sources (poles) P02c, P02b, P01c, P01a, P01b, P09, and P03; and the northern ribbon is associated with the spines connecting N07, N05, N13, N03, N02, N01, N18, N19, and N15. Field lines connecting the pairs of opposite sources listed above represent flaring domains; the nulls which lie between those sources we call flaring nulls. The calculated geometry of spines is close to the observed ribbon location to within the accuracy of the point-charge representation of the magnetic field. For example, in Figure 4, the spine which goes through N02 is not directly associated with any ribbon at 11:15 UT. However, if we look at the evolution of the ribbon position during the decaying stage of the flare (after 12:30 UT), the location of the northern ribbon goes through the southern part of region N02.

Once the set of flaring domains is found, we can estimate the amount of flux that the flaring domains exchanged. For this, we find domain fluxes in the potential field $\psi^{(v)}_{a/b}(t)$ before and after the energy buildup at t_0 and $t_{\rm flare}$. To calculate the domain fluxes, we use a Monte Carlo method (see Barnes et al. 2005) whereby field lines are initiated from point charges in random directions and followed to their opposite ends. Due to magnetic charge motions, some domains gain flux ($\Delta\psi^{(v)}_{a/b} = \psi^{(v)}_{a/b}(t_{\rm flare}) - \psi^{(v)}_{a/b}(t_0) > 0$), while the others lose flux ($\Delta\psi^{(v)}_{a/b} < 0$). Using solid and dashed lines, Figure 3 shows domains with the largest domain flux changes, i.e., $|\Delta\psi^{(v)}_{a/b}| > 0.5\times 10^{21}$ Mx. In other words, reconnection transfers flux from flaring domains for which $\Delta\psi^{(v)}_{a/b} < 0$ (dashed) and into faring domains for which $\Delta\psi^{(v)}_{a/b} > 0$ (solid). By summing all the positive and negative domain flux changes in the flaring domains and taking their absolute value, we find the net flux transfer which must occur in the two-ribbon flare: $\Delta\Psi_{\rm model} = 15.5(14.8) \times 10^{21}$ Mx. Were it not for connections outside the ribbon set with external sources, these two quantities would exactly match, since one domain's increase comes from another domains' decrease. It is this flux transferred by reconnection which was responsible for the X17 flare.

The model reconnection flux from the connectivity analysis discussed above could be compared with observed reconnection flux derived from the ribbon motion. Two flare ribbons associated with the impulsive phase of the X17 flare were observed by *TRACE* at 1600 Å with 30 s cadence and with a pixel size of 0.″5 between 09:30 and 12:50 UT. The ribbons became visible in 1600 Å images at 10:58 UT and peaked at 12:51 UT. To measure the total magnetic flux swept out by the motion of the ribbons, we count all pixels that brightened during any period of the flare and then integrate the unsigned magnetic flux encompassed by the entire area taking into account the height of the ribbon's formation, a 20% correction (Qiu et al. 2007). The total measured reconnection fluxes at 12:51 UT when the reconnection flux rate is close to zero amount to $\Delta\Psi_{\rm obs,+} = (2.6 \pm 0.5) \times 10^{22}$ Mx and $\Delta\Psi_{\rm obs,-} = (-1.9 \pm 0.3) \times 10^{22}$ Mx for positive and negative fluxes, respectively (the height of the ribbon's formation is $h = 2000$ km, the ribbon-edge cutoff is taken to be 10 times the background intensity). The model reconnection flux ($\Delta\Psi_{\rm model} = 1.5 \times 10^{22}$ Mx) compares favorably with observed reconnection flux derived from *TRACE* within the given uncertainties.

Table 1
Properties of the Flaring Separators Derived from the MCC Model, *Rotating Case*

i	Nulls		L_i	$z_{i,\max}$	$\Delta\psi_i$	I_i	$\mathcal{E}_i$	H_i
	−	+	Mm	Mm	10^{21} Mx	GAmps	10^{30} erg	10^{42} Mx^2
1	A12	B03	185.8	72.7	−1.98	−262.6	22.82	−19.81
2	A12	B04	101.8	31.4	−1.97	−548.7	46.37	−23.58
3	A09	B03	85.1	26.3	−1.67	−523.2	37.86	−17.13
4	A09	B04	74.9	24.2	−1.66	−575.3	41.49	−16.60
5	A08	B02	134.0	31.4	−0.46	−76.5	1.58	−2.55
6	A09	B02	129.3	31.6	−1.80	−469.5	35.16	−15.86
Total							185.28	−95.53

Notes. Listed are each separator's index, i, shown in Figure 5, the labels of the nulls linked by the separator (nulls), the length, L_i, and maximum height, $z_{i,\max}$, of the separator in the potential field on October 28 10:00 UT. The flux discrepancy, $\Delta\psi_i$, between that field and the initial one (October 26 12:00 UT) leads to the current I_i, which in turn leads to self-free-energy $\mathcal{E}_i$ and helicity H_i on each separator.

5. FLARE ENERGY AND FLUX ROPE HELICITY: MCC MODEL AND OBSERVATIONS

We now apply the MCC model, as described in Papers I and II, to the quadrupolar model, where the sunspot rotation is determined from the MDI intensity images. This produces an estimate of the energy and helicity available for the Halloween flare.

From the set of flaring poles and nulls, we found six flaring separators, i.e., separators connecting the flaring nulls (thick lines in Figure 5). The main properties of those separators are listed in Table 1: separator index (i, same as in Figure 5), flaring nulls that the separator connects (nulls), length (L_i), maximum height ($z_{i,\max}$), flux ($\Delta\psi_i$), current (I_i), energy ($\mathcal{E}_i$), and helicity (H_i) (as described in Appendix B in Kazachenko et al. 2009). Table 1 indicates that the most energetic separators are the lowest separators $i = 2$ (4.6×10^{31} erg), $i = 3$ (3.7×10^{31} erg), and $i = 4$ (4.1×10^{31} erg). According to *TRACE* 1600 Å ribbon observations, the flare brightening first happens in partitions P01 and N02. The separator whose nulls lie closest to those partitions is $i = 4$, which is the lowest lying one (see Table 1). As the flare progresses, the reconnection moves from separator to separator, balancing the flux and reducing the energy state of the global magnetic field (Longcope & Beveridge 2007). In the bottom row of Table 1, the total energy ($\mathcal{E}_{\rm MCC}$) and helicity ($H_{\rm MCC}$) of the reconnection sequence are given. The total helicity released on six *flaring* separators $H_{\rm MCC} \simeq -9.5 \times 10^{43}$ Mx^2 accounts for a large part of the helicity injected by the motions of the model flux sources, shown in Figure 3. The total helicity in the whole active region contributes to currents flowing in the other 26 separators, so it is somewhat larger ($\Delta H_{\rm br} = -1.4 \times 10^{44}$ Mx^2; see Equation (4)). The total energy released through a sequence of reconnections on all flaring separators is $\mathcal{E}_{\rm MCC} = 1.85 \times 10^{32}$ erg.

In the MCC model, currents are driven along separators to offset changes in the potential flux of the domains lying under these separators. The domains which lie under the flaring separators are P01a-N03, P01b-N03, P01c-N03, P01b-N02, and P02b-N03. Out of the whole set of domains those are the only ones that determine the helicity and energy content of the flux rope. It is interesting that P02b-N03 is the only P02 domain, i.e., a domain influenced by rotation; it takes part in the energetics of

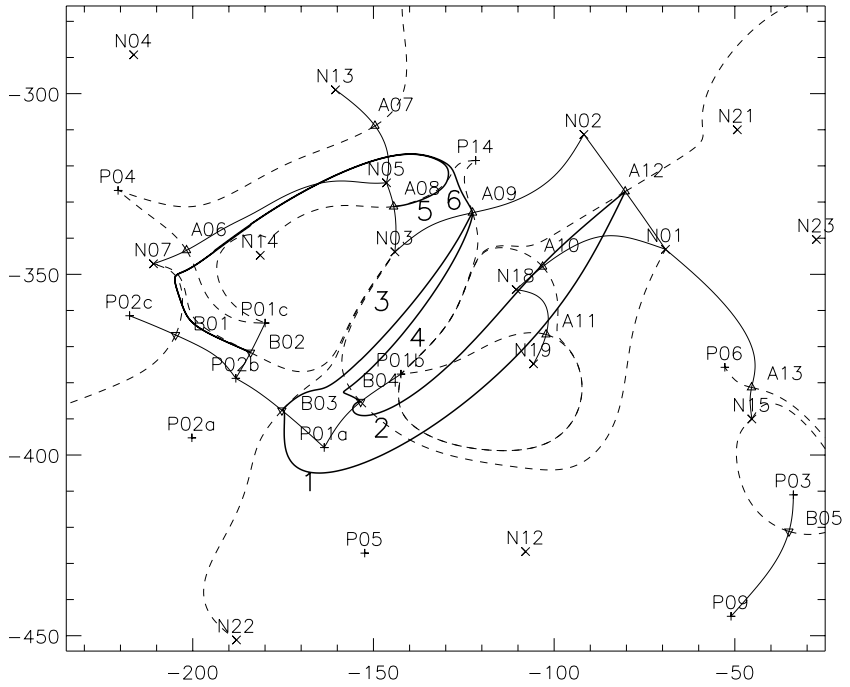

Figure 5. Elements of the topological skeleton footprint on October 28 10:00 UT, plotted on the tangent plane, see Section 4. Thin solid lines are the spine curves and dashed lines are the photospheric footprints of separatrices. Thick solid lines are flaring separators. The large numbers near each separator are the separator indices i, as in Tables 1 and 2. Axes are in arcseconds from disk center.

only one flaring separator $i = 6$ (3.5×10^{31} erg) which contains 18% of the total energy.

We may test the model by comparing the self-free-energy value computed from the MCC model to three energy values derived from the observations. First, the total radiated energy output of the flare can be estimated from the GOES observations. Using GOES analysis software in SolarSoft, the observed fluxes in the two channels (1–8 Å and 0.5–4 Å) of the GOES instrument give the plasma temperature, emission measure, and radiated power during the interval of elevated X-ray flux (Mewe et al. 1985). Integrating the radiated power over this time period gives a total radiated energy of $\mathcal{E}_{\rm obs} = 5.5 \times 10^{31}$ erg. This energy value is about three times smaller than the model value $\mathcal{E}_{\rm MCC} = 1.85 \times 10^{32}$ erg. Second, Régnier & Priest (2007) calculated the free energy of the active region as a whole using nonlinear force free and potential extrapolations of vector magnetograms $\mathcal{E}_{\rm free} = \mathcal{E}_{\rm nlff} - \mathcal{E}_{\rm pot} = 7 \times 10^{32}$ erg. This estimate is more than three times larger than our theoretical energy estimate. Third, Metcalf et al. (2005) estimated the free energy based on the magnetic virial theorem the next day after the flare of our study: $(5.7 \pm 1.9) \times 10^{33}$ erg (Metcalf et al. 2005). One must keep in mind that there are many uncertainties involved in the energy calculations. Firstly, the model used in GOES estimate assumes a fully filled isothermal plasma. Secondly, the MCC model provides a lower bound on the stored energy since it assumes an ideal quasi-static evolution and applies a small number of constraints rather than point-for-point line-tying (Longcope et al. 2001). Finally, there are uncertainties in the measurements of the rotation rate from MDI intensitygrams.

An interplanetary coronal mass ejection (ICME) was observed near Earth on October 29 11:30 UT. From in situ magnetic field observations with the *Advanced Composition Explorer* (*ACE*) spacecraft, it has been found that the interplanetary structure is a magnetic cloud (Hu et al. 2005). Using the Grad–Shafranov reconstruction method, the self-helicity associated with the Halloween flare magnetic cloud is $H_{\rm obs} = -3.0 \times 10^{43}\,{\rm Mx}^2$ (Hu et al. 2005, for a cloud length of 1 AU). From the standard Lundquist model fit, the MC's helicity is $H_{\rm obs} = -8.0 \times 10^{43}\,{\rm Mx}^2$ (Lynch et al. 2005, for a cloud length of 1 AU). One must keep in mind that both approaches have a large uncertainty since the spacecraft crossed the edge of the magnetic cloud (Q. Hu 2009, private communication, case B in Riley et al. 2004).

Our model value of the flux rope self-helicity lies between the two estimates. The liftoff of the flux rope does not remove all of the helicity available in the flux rope (Mackay & van Ballegooijen 2006). For the MHD simulated eruption, Gibson & Fan (2008) found that 41% of the helicity is lost with the escaping rope, while 59% remains. For simplicity, we assume that 50% of the total mutual helicity from the MCC model (see Table 1) ends up as self-helicity of the flux rope created by reconnection. Then the ejected flux rope would carry $H_{\rm self} = \frac{H_{\rm MCC}}{2} \simeq -4.8 \times 10^{43}\,{\rm Mx}^2$.

The focus of this paper is prediction of the energy and helicity budget produced by reconnection in the flare; we deliberately do not address the morphology. There is already an extensive literature about this matter (see review by Démoulin 2007). In the context of the methods of this paper, morphological studies have been done by Des Jardins et al. (2009a) and Des Jardins et al. (2009b). Des Jardins et al. (2009b) compared the RHESSI hard X-ray (HXR) footpoint motions of three flares with the location of topological spines and found that the HXR sources moved along the spine lines. They conclude that such motion corresponds to movement of the reconnection location.

6. THE ROLE OF ROTATION

We now seek to understand the role of sunspot rotation. For that purpose, we compare the rotating case discussed above, where three poles representing P02 rotate uniformly at a rate

Table 2
Properties of the Flaring Separators Derived from the MCC Model, *Non-rotating Case*

i	Nulls		L_i	$z_{i,\max}$	$\Delta\psi_i$	I_i	$\mathcal{E}_i$	H_i
	−	+	Mm	Mm	10^{21} Mx	GAmps	10^{30} erg	10^{42} Mx^2
1	A12	B03	185.8	72.7	−1.88	−245.4	20.31	−18.52
2	A12	B04	101.8	31.4	−1.81	−487.9	38.09	−20.97
3	A09	B03	85.1	26.3	−1.58	−487.2	33.55	−15.95
4	A09	B04	74.9	24.2	−1.51	−508.1	33.57	−14.66
5	A08	B02	134.0	31.4	−0.40	−63.9	1.15	−2.13
6	A09	B02	129.3	31.6	−1.72	−436.5	31.30	−14.75
Total							157.97	−86.96

Note. For header information, see Table 1.

of 2.°67 hr^{-1} for the 46 hr of buildup, with the non-rotating case, where the three poles P02a-c are kept at the same angle as in the magnetogram at $t_{\rm flare}$ throughout the 46 hr buildup. In the non-rotating case, P02a-c do move in order to account for the motion and distortion of P02, but by keeping the average angle between the three charges fixed they do not inject helicity due to sunspot rotation (see Appendix A of Paper II for details).

In Table 2, we list the properties of the flaring separators for the non-rotating case, for comparison, with those for the rotating case shown in Table 1. Since in both cases the topological skeleton at $t_{\rm flare}$ is the same, the geometrical properties of the flaring separators, such as length (L_i) and maximum height ($z_{i,\max}$), are also the same. However, since the topology of the magnetic field at t_0 differs in two cases, the changes in the fluxes ($\Delta\psi_i$) of the domains underlying the flaring separators and hence current (I_i), energy ($\mathcal{E}_i$), and helicity (H_i) also differ. Comparing the bottom rows of Tables 1 and 2, we see that the total energy and helicity values differ by only 10%: in the rotating case, the total energy is $\mathcal{E}_{\rm MCC} = 1.8 \times 10^{32}$ erg and the helicity is $H_{\rm MCC} \simeq -9.5 \times 10^{43}$ Mx^2; and in the non-rotating case, the energy is $\mathcal{E}_{\rm MCC} = 1.6 \times 10^{32}$ erg and the helicity is $H_{\rm MCC} \simeq -8.7 \times 10^{43}$ Mx^2. This comparison clearly indicates that rotation is not important in this event.

In fact, among the six flaring separators there is only one separator $i = 6$ which overlies a domain directly influenced by rotation, i.e., the P02b-N03 domain. However, since the P02b-N03 domain is small ($\Phi = 0.1 \times 10^{21}$ Mx) and its flux does not change much with time in either case, we get very similar properties of the separator $i = 6$ in two cases: its energy is 3.5×10^{31} erg for the rotating case and 3.1×10^{31} erg for the non-rotating case; its helicity is -1.5×10^{43} Mx^2 for the rotating case and -1.6×10^{43} Mx^2 for the non-rotating case.

The total reconnected flux, i.e., the amount of positive and negative changes in the domain flux of the flaring domains, is comparable in two cases: the non-rotating case predicts $\Delta\Psi_{\rm model} = 1.2 \times 10^{22}$ Mx of reconnected flux and the rotating case predicts $\Delta\Psi_{\rm model} = 1.5 \times 10^{22}$ Mx; earlier in Section 4, we found $\Delta\Psi_{\rm obs} = 2.6(-1.9) \times 10^{22}$ Mx of reconnected flux from measurements of the observed ribbon brightening separation. Slightly lower predictions in the non-rotating case are related to smaller, slower change in the domain flux. However, since the rotation of P02 happens far from the location where the flare happened, it does not influence the domain flux evolution and hence the separator properties enclosing those domains.

From the above comparison, we conclude that shearing motions dominate the flare energy and helicity budget of this flare.

7. CONCLUSIONS

This paper follows Papers I and II in which topological methods were applied to understand the role of sunspot rotation, in comparison to shearing, in storage of energy and helicity prior to two large eruptive flares. In the active region, harboring the X2-class 2004 November 7 flare, as Longcope et al. (2007b) showed, only shearing motions and no rotation have been observed, and shearing determined the energy budget of the flare (Paper I). In the M5.8-class 2005 May 13 flare, both rotation of the large positive sunspot and shearing motions have been observed, and that rotation clearly dominated the flare energetics (Paper II). In this paper, we analyze the Halloween X17 flare on 2003 October 28 in which both rotation of the large positive sunspot and shearing motions have been observed. We show that shearing dominates the flare helicity and energy, and rotation is not important.

NOAA 10486 has a large positive sunspot P02 containing 20% (15.7×10^{21} Mx) of the total AR's positive flux, which rotated by 123° in 46 hr before the flare. Since the total helicity flux is the sum of the braiding and spinning helicity fluxes, such a significant rotation along with a fact that the spin helicity flux is proportional to the magnetic flux squared might give an idea that rotation of P02 is important for the flare. Indeed, the fast rotating sunspot P02 is important for the helicity budget of the whole active region. We show that the rotation of P02 raises the total helicity flux of the active region by 50% (from -9×10^{43} Mx^2 to -14×10^{43} Mx^2).

Although the rotation of P02 is important for the whole active region, we conclude that it is not important for the flare. We reach this conclusion by considering the six flaring separators, which connect nulls nearest to the flare ribbons. Using the MCC model (Longcope 1996) for each separator, we find the current, generated by the changes in the underlying domain fluxes, the energy, and the helicity. Topological analysis reveals that among the domains underlying the flaring separators there is only one P02 domain. This domain is overlaid by only one flaring separator ($i = 6$), which contains less than 15% of the total energy released on all flaring separators. In other words, in spite of the fast rotation of P02, its direct contribution to the flare energetics is small. However, since there are other domains which lie under the mentioned separator and influence its energetics, to estimate the role of rotation in the flare more accurately we compare the observed case where P02 rotates (rotating case) with the hypothetical model case where P02 does not rotate (non-rotating case). We find that in the rotating case the flare energy and flux rope helicity are only 10% larger than the one in the non-rotating case. We show that the reason for that lies in the topology of the rotation relative to the flare's location. Since the rotation of P02 happens far from the location where the flare happened, it does not affect the flux changes of the domains lying under the most energetic flaring separators and hence the properties of those separators such as current, helicity, and energy.

We assume that the flux rope created in a sequence of reconnections would carry away half of the injected helicity, i.e., its self-helicity is $H_{\rm self} = \frac{H_{\rm MCC}}{2} = -4.8 \times 10^{43}$ Mx^2. The *ACE* spacecraft made observations of an ICME believed to have been launched during the flare. These measurements show a flux rope with helicity comparable to that in the model ($H_{\rm obs} = -3.0 \times 10^{43}$ Mx^2, Hu et al. 2005; $H_{\rm obs} = -8.0 \times 10^{43}$ Mx^2, Lynch et al. 2005). However, the estimate of helicity using the *ACE* data with both methods yields a large uncertainty since the spacecraft crossed the edge of the magnetic cloud

(?) Q. Hu (2009), private communication, case B in Riley et al. 2004).

Several authors have made energy estimates relevant to NOAA 10486 and the Halloween flare. Our theoretical estimate for the free magnetic energy ($\mathcal{E}_{\rm MCC} = 1.8 \times 10^{32}$ erg) is three times larger than the radiated energy loss from GOES observations ($\mathcal{E}_{\rm obs} = 5.5 \times 10^{31}$ erg). Régnier & Priest (2007) and Metcalf et al. (2005) estimated the free magnetic energy accumulated in the whole NOAA 10486 as 7×10^{32} erg and $(5.7 \pm 1.9) \times 10^{33}$ erg. Comparing the $\mathcal{E}_{\rm MCC}$ to the $\mathcal{E}_{\rm free}$ estimate by Régnier & Priest (2007), it is not surprising that the flare radiates only 25% of that contained in the whole active region. However, one must keep in mind that our energy estimate yields a lower bound on the free-energy of a line-tied field (Longcope et al. 2001). In summary, lacking a detailed model of how the energy stored as currents on the separators is converted to other forms (thermal, mass motions, and accelerated particles), we conclude that the MCC energy budget is consistent with observations and the works of other authors.

Using methods other than point charges, the topology of the NOAA 10486 has been studied by several authors (Mandrini et al. 2006; Zuccarello et al. 2009; Régnier et al. 2005). Even though their topological methods are different from the ones in this paper, the comparison is valuable. Using linear (Mandrini et al. 2006; Zuccarello et al. 2009) and nonlinear (Régnier et al. 2005) force free extrapolations of the magnetic field at different times, in all three papers a coronal magnetic null point lying above the negative polarity N07 (between P04 and P02) has been found. The observational evidence for nulls is weaker than for separators; flares may occur without being associated to null points but they will be associated to separators or, more generally, to quasi-separatrix layers (QSLs; Démoulin et al. 1994; Barnes 2007; Démoulin 2007, and references therein). While the coronal magnetic null point found by these authors could be relevant (Zuccarello et al. 2009) to the X17 flare onset, or not (Mandrini et al. 2006), we find two flaring separators ($i = 5$, $i = 6$) which lie close to it.

In addition, from a linear force-free extrapolation of the magnetogram at the flare time (11:11 UT), Mandrini et al. (2006) found QSLs, i.e., thin coronal volumes where field lines display drastic connectivity gradients (Démoulin et al. 1996), related to a precursor event. These authors claim that magnetic reconnection at these QSLs removes the stabilizing magnetic arcade above the filament, as in the breakout CME model but without a coronal null point. Visually comparing our topology with the QSL locations we speculate that, in our case, one of the QSLs would be associated with one of the two flaring separators $i = 5$ or $i = 6$. However, the goal of our analysis is to quantify the properties of the flux rope created during the X17 event itself, not the precursor event.

We thank the referee for constructive comments, which helped to improve the manuscript. We thank the *TRACE* and *SOHO* MDI teams for providing the data. *SOHO* is a project of international cooperation between ESA and NASA. We are pleased to acknowledge support from NASA Earth and Space Science Fellowship grant NNX07AU73H (M.D.K.), NASA LWS TR&T grant NNG05-GJ96G (R.C.C. and M.D.K.), and grant ATM-0748428 (M.D.K. and J.Q.).

REFERENCES

Barnes, G. 2007, ApJ, 670, L53
Barnes, G., Longcope, D. W., & Leka, K. D. 2005, ApJ, 629, 561
Berger, M. A., & Field, G. B. 1984, J. Fluid Mech., 147, 133
Chae, J. 2001, ApJ, 560, L95
Démoulin, P. 2007, Adv. Space Res., 39, 1367D
Démoulin, P., & Berger, M. A. 2003, Sol. Phys., 215, 203
Démoulin, P., Hénoux, J., & Mandrini, C. 1994, A&A, 285, 1023
Démoulin, P., Henoux, J. C., Priest, E. R., & Mandrini, C. 1996, A&A, 308, 643
Des Jardins, A., Canfield, R., Longcope, D., McLinden, E., & Dillman, A. 2009a, 693, 886D
Des Jardins, A., Canfield, R., Longcope, F. C., & Waitukaitis, S. A. 2009b, 693, 1628D
Gibson, S. E., & Fan, Y. 2008, J. Geophys. Res. (Space Phys.), 113, 9103
Hu, Q., Smith, C. W., Ness, N. F., & Skoug, R. M. 2005, J. Geophys. Res. (Space Phys.), 110, 9
Hurford, G. J., Krucker, S., Lin, R. P., Schwartz, R. A., Share, G. H., & Smith, D. M. 2006, ApJ, 644, L93
Kazachenko, M. D., Canfield, R. C., Longcope, D. W., Qiu, J., Des Jardins, A., & Nightingale, R. W. 2009, ApJ, 704, 1146
Li, C., Tang, Y. H., Dai, Y., Fang, C., & Vial, J. 2007, A&A, 472, 283
Longcope, D. W. 1996, Sol. Phys., 169, 91
Longcope, D. W. 2001, Phys. Plasmas, 8, 5277
Longcope, D. W., & Beveridge, C. 2007, ApJ, 669, 621
Longcope, D. W., Kankelborg, C. C., Nelson, J. L., & Pevtsov, A. A. 2001, ApJ, 553, 429
Longcope, D., Beveridge, C., Qiu, J., Ravindra, B., Barnes, G., & Dasso, S. 2007a,, 244, 45
Longcope, D. W., Ravindra, B., & Barnes, G. 2007b, ApJ, 668, 571
Longcope, D. W., Barnes, G., & Beveridge, C. 2009, ApJ, 693, 97
Lynch, B. J., Gruesbeck, J. R., Zurbuchen, T. H., & Antiochos, S. K. 2005, J. Geophys. Res. (Space Phys.), 110, 8107
Mackay, D. H., & van Ballegooijen, A. A. 2006, ApJ, 641, 577
Mandrini, C. H., Demoulin, P., Schmieder, B., Deluca, E. E., Pariat, E., & Uddin, W. 2006, Sol. Phys., 238, 293
Metcalf, T. R., Leka, K. D., & Mickey, D. L. 2005, ApJ, 623, L53
Mewe, R., Gronenschild, E. H. B. M., & van den Oord, G. H. J. 1985, A&AS, 62, 197
November, L. J., & Simon, G. W. 1988, ApJ, 333, 427
Pariat, E., Démoulin, P., & Berger, M. A. 2005, 439, 1191
Pick, M., Malherbe, J., Kerdraon, A., & Maia, D. J. F. 2005, ApJ, 631, L97
Qiu, J., & Gary, D. E. 2003, ApJ, 599, 615
Qiu, J., Hu, Q., Howard, T. A., & Yurchyshyn, V. B. 2007, ApJ, 659, 758
Régnier, S., Fleck, B., Abramenko, V., & Zhang, H.-Q. 2005, ESA Special Publication, 596
Régnier, S., & Priest, E. R. 2007, ApJ, 669, L53
Riley, P., et al. 2004, J. Atmos. Sol.-Terr. Phys., 66, 1321
Scherrer, P. H., et al. 1995, Sol. Phys., 162, 129
Schmieder, B., Mandrini, C., Berlicki, A., Démoulin, P., & Li, H. 2006, in SOHO-17. 10 Years of SOHO and Beyond
Schrijver, C. J., et al. 2006, 235, 161
Su, Y. N., Golub, L., van Ballegooijen, A. A., & Gros, M. 2006, Sol. Phys., 236, 325
Trottet, G., Krucker, S., Lüthi, T., & Magun, A. 2008, ApJ, 678, 509
van Driel-Gesztelyi, L., Démoulin, P., & Mandrini, C. H. 2003, Adv. Space Res., 32, 1855
Welsch, B. T., & Longcope, D. W. 2003, ApJ, 588, 620
Zhang, M., Flyer, N., & Low, B. C. 2006, ApJ, 644, 575
Zuccarello, F., et al. 2009, A&A, 493, 629